

MOVING-TARGET VELOCITY ESTIMATION IN A COMPLEX-VALUED SAR IMAGERY

Yuan Li¹, Gaohuan Lv^{2, *}, and Xingzhao Liu²

¹School of Computer Science and Technology, Shandong Institute of Business and Technology, 191 Binhai Road, Yantai 264005, China

²Department of Electronic Engineering, Shanghai Jiao Tong University, 800 Dongchuan Road, Shanghai 200240, China

Abstract—In the ground moving target indication with synthetic aperture radar (SAR) community, algorithms used to estimate the velocity of a detected moving target are important because they are relative to the topics about refocusing and azimuth displacement correction. The velocity is regarded as a vector with two components, one in azimuth and one in range direction, and new algorithms aiming at estimating the two components are proposed and verified. The range velocity estimator transforms a detected patch containing a moving target to range Doppler domain by using the 1-D fast Fourier Transform in each range bin to achieve its range Doppler locus. The slope of the range Doppler locus is computed by using the Radon Transform on the range Doppler plane and the range velocity component is worked out according to radar system parameters and the slope value. Two estimators are proposed to compute the azimuth velocity component. One is based on symmetric defocusing in Doppler domain, the other is based on phase gradient in wave-number domain. Experiments confirm the effectiveness of the estimators by using simulated and field data.

1. INTRODUCTION

Moving target detection, imaging, and velocity estimation are active research fields with civilian and military applications in synthetic aperture radar (SAR) community [1–13]. Many applications aim at determining the position and the velocity of certain targets. It is critical to estimate its velocity because properly refocusing and locating

Received 20 November 2012, Accepted 9 January 2013, Scheduled 19 January 2013

* Corresponding author: Gaohuan Lv (lvgh@sjtu.edu.cn).

the moving target require the knowledge of the two components. This paper address the design of processing algorithms aiming at estimating the velocity of a detected moving target in a complex-valued SAR imagery.

Traditional velocity estimators use multi-antenna systems, such as linear antenna array velocity SAR (VSAR) [14], along-track interferometry [4, 10, 15–17], and displaced-phase-center-antenna [8, 18]. They can give accurate velocity estimate and resolve the velocity ambiguity well. However, the systems are so complex that both hardware and computation efforts are needed. Many velocity estimators based on a single antenna SAR or a complex-valued SAR imagery are proposed to overcome the shortcomings inherent in the multi-antenna systems. Most of them are based on the azimuth phase history originated by moving targets [8, 19–23]. In addition, some meaningful works that take into account the antenna radiation pattern are also effective [3, 24, 25]. Estimators herein are designed based on the azimuth phase history.

It is known that a moving target's range and azimuth motion influence its Doppler shift and Doppler rate in the azimuth phase history, respectively. Accordingly, the velocity estimation problem is equal to determining the two Doppler parameters naturally. Due to temporal sampling, the induced Doppler shift suffers the limitation of pulse repetition frequency (PRF). Classical solutions to this problem are to relocate the equipment with an increasing PRF [2] or a nonuniform PRF [26], or using waveform diversity techniques [27]. However, these measures increase the memory requirement and equipment complexity.

Many methods are proposed to improve the dilemma successively. Kirsht estimates the velocity by evaluating the variation of the single amplitude during the sequence with sub-aperture technique [21]. This approach relies on thorough measurement of the moving target position and amplitude. However, the requirement is hard to be fulfilled in practice. J. Dias et al. use the antenna radiation pattern information to determine the range velocity from the skew of the two-dimensional spectral signature of a moving target, and determine the azimuth velocity component from the scale of the antenna radiation patten [3, 24, 25]. These methods give effective results when the moving target signatures are digitally spotlighted. However, it is suitable for a point-like moving target, when the Doppler locus of a moving target is mixed with that of background, or an extended moving target exists, the estimation accuracy can not be ensured. S. Brush et al. estimate the velocity vector by azimuth split decomposition, i.e., spectrum bandpass filtering [28]. In this method, the azimuth velocity

component depends on the estimation accuracy of the displacement vector, and the range velocity component depends on the estimation accuracy of the temporal shift and the local incident angle. A newer estimator based on the range alignment method is proposed by Wang et al. [23]. It exploits the fact that range migration can be corrected by shifting the Doppler slices such that their envelopes are similar, and thus the Doppler centroid can be estimated from the shifting step. This estimator also suffers from small signal-to-clutter ratio.

We propose new velocity estimators for a detected moving target in a complex-valued SAR imagery based on the symmetric de-focusing technique. The basic idea is the combination of azimuth phase history and fundamental kinematics. To be specific, the Doppler locus of a moving target appears as an oblique line in the range Doppler plane due to the range motion, and a coarse range velocity component can be deduced from the slope of the oblique line and radar system parameters.

Due to the azimuth motion, the image of a moving target will be smeared in azimuth direction when its returns are processed in the same way as the stationary returns. Processed by two symmetric defocusing filters (SDF), the target image derives two defocused versions. In the two defocused images, the background is defocused to the same extent, while the moving target is defocused in different degrees. The sharpness difference between the two defocused images is used as a feature value to estimate the azimuth velocity component with an SDF bank. The feature value is robust because it tries to alleviate the influence of the clutters and interferences. Another azimuth velocity estimator (AVE) is based on phase gradient technique in Doppler domain. In each range bin of the range Doppler plane, the phase gradient appears as a oblique line due to the azimuth motion. Combining the slope of the oblique line with radar system parameters, the azimuth velocity estimate works out. This estimator can get high estimation accuracy under condition of a strong moving target or a large PRF. However, it is not robust when a weak moving target is embedded in strong background.

The paper is organized as follows. In Section 2, radar imaging fundamentals are introduced briefly. Section 3 describes a range velocity estimator based on Radon transform on the range Doppler plane. Then two AVEs based on an SDF bank and phase gradient technique are described in Sections 4 and 5, respectively. In Section 6, experiments are presented to show the effectiveness of the proposed algorithms by using simulated and field data. Finally, Section 7 draws a conclusion.

2. FUNDAMENTALS

2.1. Kinematics and Range Doppler Plane

A typical slant-plane of a bore-sight strip-map SAR scenario is shown in Figure 1. A moving target is located at $(R_0, 0)$ when it is in the antenna bore-sight direction. It moves at a constant velocity V_a in azimuth and a constant velocity V_r in range. The radar platform moves with a constant velocity V_p . θ_B is the antenna beam-width and $\Delta\eta$ is the time interval during which the target travels through one range bin. During the imaging period, the target is located at range bin r_0 when the radar beam arrives at time $\eta = -\eta_0$, and at range bin r_{N-1} when the beam departs at time $\eta = \eta_0$.

The distance from platform to target at time η is

$$R(\eta) = \sqrt{(R_0 + V_r\eta)^2 + (V_p - V_a)^2\eta^2} \approx R_0 + V_r\eta + \frac{(V_p - V_a)^2\eta^2}{2R_0}, \quad |\eta| \leq \eta_0 \quad (1)$$

Ignoring the constant phase term, the Doppler phase history can be written as

$$\phi(\eta) = 2\pi f_{dc}\eta + \pi f_{dr}^m \eta^2, \quad |\eta| \leq \eta_0 \quad (2)$$

where $f_{dc} = -2V_r/\lambda$, $f_{dr}^m = -2(V_p - V_a)^2/(\lambda R_0)$, and λ denotes the carrier wavelength. As one range bin length is

$$\Delta r = \frac{c}{2f_s}, \quad (3)$$

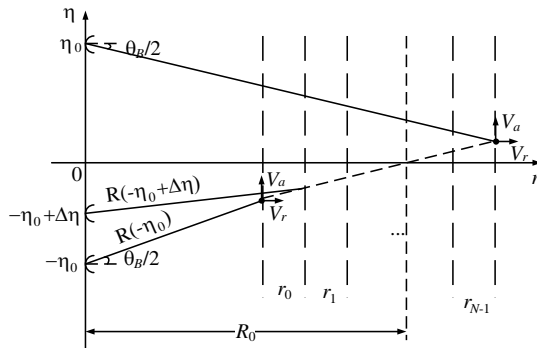


Figure 1. A sketch of typical strip-map SAR scenario with a moving target.

where c is the light speed, and f_s is sampling frequency in the fast time domain, the moving-target-introduced Doppler phase history in the k -th range bin becomes

$$\phi_k(\eta) = \phi(\eta), \quad \left| \eta - \left(\eta_0 - \frac{\Delta\eta}{2} - k\Delta\eta \right) \right| \leq \frac{\Delta\eta}{2} \quad (4)$$

where $\Delta\eta = c/(2f_s V_r)$. The Doppler centroid in (4) is

$$f_{dc}^{(k)} = f_{dc} + \left(\eta_0 - \frac{\Delta\eta}{2} - k\Delta\eta \right) f_{dr}^m, \quad (5)$$

and the Doppler rate is

$$f_{dr}^{(k)} = f_{dr}^m. \quad (6)$$

It can be seen that the distance between the Doppler centroids of the moving target in two adjacent range bins is

$$\Delta f_{dc} = f_{dc}^{(k+1)} - f_{dc}^{(k)} = -f_{dr}^m \Delta\eta, \quad (7)$$

and the Doppler bandwidth in the range bin r_k is

$$B_D^{(k)} = -f_{dr}^m \Delta\eta, \quad (8)$$

which means that in a synthetic aperture time, the Doppler bandwidth of a moving target can be written as

$$B_D = N B_D^{(k)} = \frac{2(V_p - V_a)\theta_B}{\lambda}. \quad (9)$$

Figure 2 shows a sketch of Doppler loci of different targets in a range Doppler plane. T_1 represents the Doppler locus introduced by a stationary target, and it appears as a straight line perpendicular to

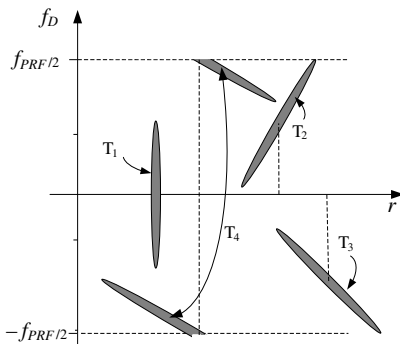


Figure 2. A sketch of range Doppler plane.

the range axis. T_2 represents that of a target moving towards the radar, and it appears as an oblique line having a positive slope. T_3 represents that of a target moving backwards the radar, and it appears as an oblique line having a negative slope. T_4 represents a target moving backwards from the radar so fast that its Doppler locus appears in the form of two separated parts wrapping around pulse repetition frequency. It can be seen that the slope of the Doppler locus varies with the range velocity component of the moving target, and thus the range velocity component value can be deduced from the slope of the corresponding Doppler locus roughly.

2.2. Radar Image of a Moving Target

Without considering the antenna beam-pattern, the azimuth signal history of a moving target in the range bin r_k can be approximately written as

$$s_m^{(k)}(\eta; \mathbf{V}_m) = e^{j\phi_k(\eta)}, \quad \left| \eta - \left(\eta_0 - \frac{\Delta\eta}{2} - k\Delta\eta \right) \right| \leq \frac{\Delta\eta}{2} \quad (10)$$

where $\mathbf{V}_m = (V_r, V_a)$. By taking the Fourier transform of (10), the signal history in Doppler domain can be expressed by

$$S_m^{(k)}(f_D; \mathbf{V}_m) = \gamma e^{-j\pi k_m f_D^2} e^{-j2\pi f_D(\eta_0 - f_{dc} k_m)}, \quad \left| f_D - f_{dc}^{(k)} \right| \leq \frac{B_D^{(k)}}{2} \quad (11)$$

where $k_m = 1/f_{dr}^m$, $\gamma = e^{-j\pi k_m f_{dc}^{(k)2} + j2\pi f_{dc}^{(k)} \eta_0}$ is a constant, and f_D is the Doppler frequency. According to the range Doppler imaging algorithm, the azimuth matched filter

$$H_0(f_D) = e^{j\pi k_s f_D^2} \quad (12)$$

where $k_s = -\lambda R_0 / (2V_p^2)$, is used to compress the azimuth signal in each range bin.

Filtered by (12), signal (10) becomes

$$s_m^{c(k)}(\eta) = \frac{\sin \left[\frac{B_D^{(k)}}{2} \left(\eta - \eta_0 + \frac{V_r R_0}{V_p^2} \right) \right]}{\pi \left[\eta - \left(\eta_0 - \frac{V_r R_0}{V_p^2} \right) \right]} * s_{\text{diff}}^{(k)}(\eta), \quad (13)$$

$$s_{\text{diff}}^{(k)}(\eta) = \mathcal{F}_{f_D \rightarrow \eta} \left[e^{-j\pi \alpha_m k_s f_D^2} \right], \quad |f_D| \leq B_D^{(k)}/2$$

where $\alpha_m = k_m/k_s - 1$, and the symbol “*” means the convolution operation. It is observed that the range velocity component introduces a time-delay term and results in a misplacement by $\Delta a = -V_r R_0 / V_p$

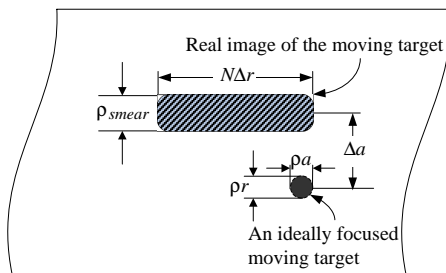


Figure 3. Ideally focused and unfocused images of a moving target.

in azimuth, and that the azimuth velocity component stretches the effective time width of the compressed signal to

$$\eta_w \approx \frac{N\lambda}{2\theta_B V_p} + |\alpha_m| \frac{R_0 \theta_B N}{V_p}. \tag{14}$$

So, the corresponding smeared image length is

$$\rho_{smear} \approx \rho_a N + |\alpha_m| \frac{N\lambda R_0}{2\rho_a}, \tag{15}$$

where $\rho_a = \lambda/(2\theta_B)$ is the azimuth resolution. Equation (15) shows that the image of the moving target is smeared approximately in $N [1 + |\alpha_m| \lambda R_0 / (2\rho_a^2)]$ azimuth resolution cells when its azimuth returns are compressed by (12) in each range bin. Figure 3 presents the comparison between the smeared and ideally focused image of a moving point target. We see that if the ideal target image occupies an area with range resolution ρ_r and azimuth resolution ρ_a , then its smeared image will cover an area with the range length $N\Delta r$ and azimuth length ρ_{smear} . In addition, the smeared image is displaced in azimuth by Δa due to the range motion.

For a quadratic phase error, in the smeared image the energy tends to be spread uniformly over the distance of the smear for an unweighted aperture, and the sharpness of target image achieves its maximum value when the moving target is ideally focused [29], which makes it possible to estimate its azimuth velocity component by using symmetric defocusing filters.

3. RANGE VELOCITY ESTIMATOR

3.1. Principle

The Radon transform has been successfully used in SAR image processing for its advantageous property in detecting lines with

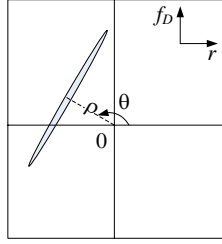


Figure 4. Geometry parameters used in Radon transform.

arbitrary orientation [30]. We adopt the Radon transform to get the slope of the Doppler locus of a moving target in the range Doppler plane. This transform integrates intensity along every possible direction in the range Doppler image and maps this information into a feature space parameterized by the angle with respect to the positive r axis, θ , and the distance from the center of the image, ρ , as shown in Figure 4.

If the discrete version of the range Doppler plane is denoted by $S_m(f_{Dm}, r_n)$, then taking Radon transform of $S_m(f_{Dm}, r_n)$, we get the Radon plane

$$S_R(\rho_n, \theta_l) = \sum_{m=0}^{M-1} \sum_{k=0}^{N-1} S_m(f_{Dm}, r_k) \text{rect} \left(\frac{\rho_n - k \cos \theta_l - m \sin \theta_l}{\Delta \rho} \right), \quad (16)$$

where $\theta_l = 2\pi l/L$, $\rho_n = n\rho_{\max}/(2K)$, $\Delta \rho = \rho_{\max}/(2K)$, and $\rho_{\max} = \sqrt{M^2 + N^2}/2$. In the Radon plane, most large values concentrate near the slope angle of the Doppler locus.

A feature used to identify the angle θ is defined by the standard deviation of $S_R(\rho_n, \theta_l)$ along dimension ρ , i.e.,

$$D(\theta_l) = \sqrt{\frac{\sum_{n=-K+1}^K |S_R(\rho_n, \theta_l) - \bar{S}_R(\theta_l)|^2}{2K}}, \quad (17)$$

$$\bar{S}_R(\theta_l) = \frac{1}{2K} \sum_{n=-K+1}^K S_R(\rho_n, \theta_l), \quad (18)$$

and the angle θ corresponding to the Doppler locus of a moving target can be simply calculated from

$$\hat{\theta} = \arg \max_{\theta_l} D(\theta_l). \quad (19)$$

As the Doppler locus of the moving target has the slope $-\tan \hat{\theta}$,

the following relationship

$$\frac{f_{dr}^s}{V_r} = -\text{ctan}\hat{\theta} \cdot \frac{\Delta f_D}{\Delta r} \tag{20}$$

provides a chance to compute a coarse range velocity component by

$$\hat{V}_r = -\text{tan}\hat{\theta} \cdot \frac{V_p^2 M f_c}{f_{\text{PRF}} f_s R_0}, \tag{21}$$

where $\Delta f_D = f_{\text{PRF}}/M$. This coarse estimate is used to align the range Doppler locus of a moving target. After the azimuth velocity estimate, say \hat{V}_a , is calculated on the aligned range Doppler plane, the final range velocity estimate will be

$$\hat{V}_r = -\text{tan}\hat{\theta} \frac{(V_p - \hat{V}_a)^2 M f_c}{f_{\text{PRF}} f_s R_0}. \tag{22}$$

3.2. Discussion

The Equation (22) can be used to estimate any range velocity in theory given that the slope of the Doppler locus is achieved. However, it is constrained by many factors actually. The equation shows that if the radar system parameters and R_0 are determined, then the estimation error of V_r is influenced by θ and V_a . Let $c_s = M f_c / (f_{\text{PRF}} f_s R_0)$, the deviation of V_r is

$$dV_r = -c_s (V_p - V_a)^2 \cdot \frac{d\theta}{\cos^2 \theta} + \text{tan}\theta \cdot c_s (V_p - V_a) dV_a. \tag{23}$$

It can be seen that dV_r is dominated by θ . θ must be in some range so that $d\theta$ and dV_a can not make the dV_r very large. In the first term of (23), as $c_s (V_p - V_a)^2$ is always larger than 1, θ is not easy to be controlled. We choose a medium range that $|\theta| \leq \pi/4$ in the research. In the last term of (23), θ should satisfy

$$|\theta| \leq \arctan\left(\frac{1}{c_s V_p}\right). \tag{24}$$

So, θ will be chosen from

$$|\theta| \leq \min\left\{\frac{\pi}{4}, \arctan\left(\frac{1}{c_s V_p}\right)\right\}. \tag{25}$$

If an estimate of θ is larger than $\pi/4$, the number of azimuth bins of the selected patch, i.e., M , should be adjusted until (25) is satisfied. In this mean, the maximum range velocity estimate is

$$|V_{r,\text{max}}| \approx c_s V_p^2. \tag{26}$$

In addition, the estimation accuracy of θ is influenced by the background. If the background is strong, then the range Doppler plane will be dominated by the background, and thus θ will not be estimated accurately. In this circumstance, the patch should be preprocessed by the clutter-excluding algorithms.

4. AN AZIMUTH VELOCITY ESTIMATOR BASED ON SYMMETRIC DEFOCUS FILTER BANK

4.1. Principle

After a target patch is compensated with the range velocity estimate \hat{V}_r , a new azimuth matched filter

$$H(f_D, \alpha) = e^{j\pi k_s(1+\alpha)f_D^2} \quad (27)$$

is used to defocus the compensated patch. As a result, the defocused image of the moving target will smear in

$$M(\alpha, \alpha_m) = 1 + |\alpha - \alpha_m| \frac{\lambda R_0}{2\rho_a^2} \quad (28)$$

azimuth resolution cells approximately. As described in [?], the combination of $H(f_D, \alpha)$ and $H(f_D, -\alpha)$ is termed an SDF pair. Two defocused versions will be generated when the compensated patch is processed by an SDF pair. If the filter $H(f_D, \alpha)$ focuses a moving target with an azimuth velocity ΔV_a ideally, then when it is used to focus the moving target with an azimuth velocity V_a , Equation (28) becomes

$$M(\Delta V_a, V_a) = 1 + \frac{|V_a - \Delta V_a| \lambda R_0}{V_p \rho_a^2}. \quad (29)$$

Many measurements are proposed to characterize the focus effective of the SAR images, such as sharpness, contrast, and entropy [23]. In this research, we choose sharpness measurement for its simplicity in computation and that it can give distinctive difference between the two defocused images. For simplicity, we assume that the patch contains a moving target and a stationary point target (background), and the two targets have the intensity $|b|^2$ and $|g|^2$, respectively. The two defocused patches herein are denoted by P_1 and P_2 . The patch P_1 has the sharpness

$$S_{p1} = \frac{|b|^4}{M(\Delta V_a, V_a)} + \frac{|g|^4}{M(\Delta V_a, 0)}, \quad (30)$$

and P_2 has the sharpness

$$S_{p2} = \frac{|b|^4}{M(-\Delta V_a, V_a)} + \frac{|g|^4}{M(\Delta V_a, 0)}. \quad (31)$$

The sharpness difference between P_1 and P_2

$$f(\Delta V_a) = \frac{|b|^4}{M(\Delta V_a, V_a)} - \frac{|b|^4}{M(-\Delta V_a, V_a)} \tag{32}$$

will be used as a feature to estimate the azimuth velocity component.

Let's discuss (32). Allowing for the symmetry of the SDF pair, we discuss it under condition of $\Delta V_a > 0$. When the azimuth velocity of a moving target, V_a , is greater than zero, two cases will appear.

1) In the case of $0 < \Delta V_a \leq V_a$, the differential of $f(\Delta V_a)$ is

$$\frac{df(\Delta V_a)}{d\Delta V_a} = \frac{2\lambda R_0 V_p \rho_a^2 |b|^4 [(V_p \rho_a^2 + \lambda R_0 V_a)^2 + (\lambda R_0 \Delta V_a)^2]}{[(V_p \rho_a^2 + \lambda R_0 V_a)^2 - (\lambda R_0 \Delta V_a)^2]^2} > 0.$$

2) In the case of $\Delta V_a > V_a$, the differential of $f(\Delta V_a)$ is

$$\frac{df(\Delta V_a)}{d\Delta V_a} = -\frac{4\lambda^2 R_0^2 V_a V_p \rho_a^2 |b|^4 (V_p \rho_a^2 + \lambda R_0 \Delta V_a)}{[(V_p \rho_a^2 + \lambda R_0 \Delta V_a)^2 - (\lambda R_0 V_a)^2]^2} < 0.$$

The two cases show that 1) when $0 < \Delta V_a \leq V_a$, the sharpness difference is a monotonic increasing function and it reaches the maximum value at the point where $\Delta V_a = V_a$, and that 2) when $\Delta V_a > V_a$, the sharpness difference is a monotonic decreasing function and it reaches the maximum value at the point where $\Delta V_a = V_a$. In addition, it infinitely approaches zero with the increment of ΔV_a .

In the case of $V_a < 0$, the following conclusions can be drawn: 1) when $0 < \Delta V_a \leq -V_a$, the sharpness difference is a monotonic decreasing function and it reaches the minimum value at the point where $\Delta V_a = -V_a$, and 2) when $\Delta V_a > -V_a$, the sharpness difference is a monotonic increasing function and it reaches the minimum value at the point where $\Delta V_a = V_a$. In addition, it infinitely approaches zero with the decrement of ΔV_a .

Figure 5 presents a sketch of $f(\Delta V_a)$ for two cases: $V_{a1} > 0$ (target 1) and $V_{a2} < 0$ (target 2). We see that the maximum sharpness difference is located at the point where $\Delta V_a = |V_a|$. If the maximum sharpness difference is less than zero, then the corresponding target is moving in the opposite direction of the platform. If the maximum sharpness difference is larger than zero, then the target is moving in the same direction of the platform.

From the discussions above, the azimuth velocity estimator can be modeled by

$$\hat{V}_a = \arg \max_{\Delta V_a} f(\Delta V_a). \tag{33}$$

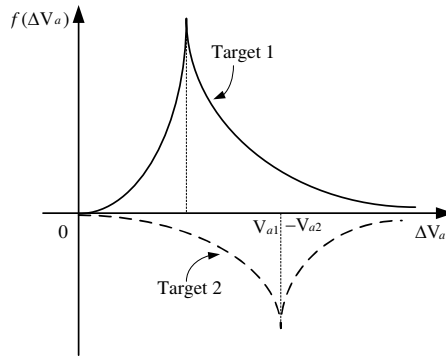


Figure 5. A sketch of sharpness difference as functions of ΔV_a .

4.2. Discussion

Let us discuss the minimum detectable azimuth velocity component $V_{\min,a}$. It is relative to the threshold value of sharpness difference which is used to identify the moving target area. According to our experience and simulation results, the sharpness difference of the two defocused images defined by $f(i, j)$ follows a half positive Gaussian distribution approximately

$$p(f) = \frac{2}{\sqrt{2\pi}\sigma} e^{-\frac{f^2}{2\sigma^2}}, \quad f \geq 0 \tag{34}$$

So, from

$$P_F = \frac{2}{\sqrt{2\pi}\sigma} \int_{f_{th}}^{\infty} e^{-\frac{f^2}{2\sigma^2}} df = \text{erfc} \left(\frac{f_{th}}{\sqrt{2}\sigma} \right) \tag{35}$$

we see that if a constant false alarm ratio P_F is given, the threshold value f_{th} can be determined.

The parameter σ in (34) can be easily calculated by using statistical theory. As $V_{\min,a} \ll V_p$, we have $\alpha_{\min} \approx 2V_{\min,a}/V_p$. Let f_{\max} denote the sharpness of the ideally focused target, and the sharpness of a moving target with azimuth velocity $V_{\min,a}$ will be

$$f_{\min,a} = \frac{f_{\max}}{1 + \frac{\alpha_{\min} \lambda R_0}{\rho_a^2}} \tag{36}$$

in the SAR image having focused background. As $f_{\min,a} \geq f_{th}$, α_{\min} approximately satisfies

$$1 - \frac{1}{1 + \frac{\alpha_{\min} \lambda R_0}{\rho_a^2}} \geq \frac{f_{th}}{f_{\max}}. \tag{37}$$

As a result, the minimum detectable azimuth velocity is approximately

$$|V_{\min,a}| \approx \frac{\epsilon \rho_a^2 V_p}{2(1 - \epsilon)\lambda R_0}, \quad (38)$$

where $\epsilon = f_{\text{th}}/f_{\text{max}}$.

5. AN AZIMUTH VELOCITY ESTIMATOR BASED ON PHASE GRADIENT

5.1. Principle

For simplicity, the analysis turns to wavenumber domain. The ideal azimuth signal history of a moving target can be written in space domain as

$$\tilde{g}(u) = ba(u - \epsilon_a u) e^{-j \frac{4\pi}{\lambda} \left[R_0 + \epsilon_r u + \frac{(1 - \epsilon_a)^2 u^2}{2R_0} \right]} \text{rect} \left(\frac{u - \epsilon_a u}{l_s} \right), \quad (39)$$

where $u = V_p \eta$ is the azimuth position of the radar, b the scattering coefficient of the target, $a(u)$ the antenna radiation pattern in azimuth direction, $\epsilon_r = V_r/V_p$, $\epsilon_a = V_a/V_p$, and l_s the synthetic aperture length. Without considering the constant phase terms, Equation (39) takes the following form in wavenumber domain

$$\tilde{G}(k_u) = bW(k_u - k_{WC}) e^{-j \frac{4\pi R_0}{\lambda}} e^{j \frac{(k_u - k_{WC})^2}{4\pi(1 - \epsilon_a)^2 K_a}}, \quad (40)$$

where $k_{WC} = 4\pi\epsilon_r/\lambda$, $W(k_u - k_{WC})$ is the antenna radiation pattern, and $K_a = 2/(\lambda R_0)$. In the n -th range bin, the azimuth signal of background is

$$\tilde{C}_n(k_u) = B_n(k_u) e^{j \frac{k_u^2}{4\pi K_a}}, \quad (41)$$

where $B_n(k_u)$ is the combination of antenna pattern and the background. The azimuth signal in the n -th range bin is

$$\tilde{S}_n(k_u) = \tilde{G}(k_u) + \tilde{C}_n(k_u). \quad (42)$$

Usually $|\epsilon_a| \ll 1$, so $1/(1 - \epsilon_a)^2 \approx 1 + 2\epsilon_a$, and thus after filtered by

$$H(k_u) = e^{-j \frac{k_u}{4\pi K_a}}, \quad (43)$$

Equation (42) becomes

$$\begin{aligned} S_n(k_u) &= bW(k_u - k_{WC}) e^{j\phi_L(k_u)} e^{j \frac{\epsilon_a k_u^2}{2\pi K_a}} + B_n(k_u), \\ \phi_L(k_u) &= \frac{(1 + 2\epsilon_a)k_{WC}^2 - 2k_{WC}(1 + 2\epsilon_a)k_u}{4\pi K_a}. \end{aligned} \quad (44)$$

It can be seen that $\phi_L(k_u)$ is a linear function of k_u , and the phase term $\varepsilon_a k_u^2 / (2\pi K_a)$ can be looked on as an interference to $\phi_L(k_u)$. It means that

$$\bar{G}(k_u, k_{WC}, \varepsilon_a) = bW(k_u - k_{WC}) \exp[\phi_L(k_u)] \quad (45)$$

denotes the azimuth history of an ideal focused moving target. Equation (44) can be rewritten as

$$S_n(k_u) = \bar{G}(k_u, k_{WC}, \varepsilon_a) e^{j \frac{\varepsilon_a k_u^2}{2\pi K_a}} + B_n(k_u), \quad (46)$$

and its discrete form is

$$S_n(k) = \bar{G}(k) e^{j \frac{\varepsilon_a k^2 \Delta k_u^2}{2\pi K_a}} + B_n(k), \quad (47)$$

where $\Delta k_u = 2\pi f_{\text{PRF}} / (MV_p)$ with M being the azimuth number of a given SAR image.

It is possible to estimate the phase difference between adjacent Doppler bins in wavenumber domain by computing the phase of

$$D_n(k) = S_n(k+1)S_n^*(k). \quad (48)$$

Substitution of (47) into (48) gives

$$D_n(k) = b^2 |W(k - k_c)|^2 e^{-j \frac{k_c(1+2\varepsilon_a)\Delta k_u^2}{2\pi K_a}} e^{j \frac{\varepsilon_a(2k+1)\Delta k_u^2}{2\pi K_a}} + B'(k), \quad (49)$$

where $k_c = k_{WC} / \Delta k_u$. The phase of $D_n(k)$ is a linear function of k corresponding to the coefficient $\varepsilon_a \Delta k_u^2 / (\pi K_a)$.

If the detected area covers L pixels in azimuth, then the ordinary least squares estimator of ε_a in the n -th range bin, i.e., $\hat{\varepsilon}_{a,\text{LS}}^{(n)}$, can be obtained from

$$\hat{\varepsilon}_{a,\text{LS}}^{(n)} = \frac{\pi K_a}{(L-2)\Delta k_u^2} \left\langle \sum_{l=0}^{L-3} \angle \left[\frac{D_n(l+1)D_n^*(l)}{|D_n(l+1)D_n^*(l)|} \right] \right\rangle. \quad (50)$$

To avoid suffering from wrapping problems, $\hat{\varepsilon}_{a,\text{LS}}^{(n)}$ is usually written as

$$\hat{\varepsilon}_{a,\text{LS}}^{(n)} = \frac{\pi K_a}{(L-2)\Delta k_u^2} \left\langle \sum_{l=0}^{L-3} \left[\frac{D_n(l+1)D_n^*(l)}{|D_n(l+1)D_n^*(l)|} \right] \right\rangle. \quad (51)$$

The variance of $\varepsilon_{a,\text{LS}}^{(n)}$ is

$$\sigma_n^2 = \frac{\pi^2 K_a^2 (1 - |\gamma_n|^2)}{2\Delta k_u^4 |\gamma_n|^2}, \quad (52)$$

where γ_n is the mean signal coherence in the n -th range bin

$$|\gamma_n|^2 = \frac{\sum_{l=0}^{L-3} |D_n(l+1)D_n^*(l)|^2}{\sum_{l=0}^{L-3} |D_n(l+1)|^2 \sum_{l=0}^{L-3} |D_n(l)|^2}. \quad (53)$$

If the Doppler locus of the moving target occupies N_r range bins after compensated by the estimated range velocity component, then two ways can be used to compute the global estimate of ε_a . One is the least square (LS) method which gives

$$\hat{\varepsilon}_{a,LS} = \frac{1}{N_r} \sum_{n=1}^{N_r} \varepsilon_{a,LS}^{(n)}. \tag{54}$$

Its variance is

$$\sigma_{LS}^2 = \frac{1}{N_r^2} \sum_{n=1}^{N_r} \sigma_n^2. \tag{55}$$

The other is the maximum likelihood (ML) method which gives

$$\hat{\varepsilon}_{a,ML} = \frac{\sum_{n=1}^{N_r} \sigma_n^{-2} \varepsilon_{a,LS}^{(n)}}{\sum_{n=1}^{N_r} \sigma_n^{-2}}. \tag{56}$$

Its variance is

$$\sigma_{ML}^2 = \left(\sum_{n=1}^{N_r} \sigma_n^2 \right)^{-1}. \tag{57}$$

5.2. Discussion

Both (50) and (51) are influenced by the clutters. Though ε_a is a constant, it varies with different background when it is computed by the function “phase(·)” in MATLAB[®]. In the experiments, the value of $\varepsilon_{a,LS}^{(n)}$ differs from each other for the same target in each range bin. The phase ambiguity influences the estimation accuracy seriously.

The slope of the phase values in

$$\phi_n(k) = \angle D_n(k) \tag{58}$$

is almost a constant in each range bin in the area covered by the Doppler spectrum of the moving target. In practice, we get the slope value k_n corresponding to the phase difference part of the moving target in the n -th range bin. As a result, the azimuth velocity can be get from

$$\varepsilon_a = k_n \frac{\pi K_a}{\Delta k_u^2}. \tag{59}$$

By combining ε_a 's in all the relative range bins, an azimuth velocity estimate can be obtained from (54) and (56).

Table 1. System parameters of simulated and field data.

Description	Value	
	Simulation	Field Data
Range to scene center	10000 m	40800 m
Platform velocity	200 m/s	218 m/s
PRF	2000 Hz	1200 Hz
Carrier frequency	10 GHz	9.6 GHz
Signal bandwidth	200 MHz	400 MHz
Sampling frequency	500 MHz	480 MHz
Range Resolution	1.0 m	0.5 m
Azimuth Resolution	1.0 m	0.5 m

A precondition is made that $|\varepsilon_a| \ll 1$ in (44). However, when ε_a is not so small, the estimated value should be modified in practice. From the algebraic function

$$\frac{1}{(1 - \varepsilon_a)^2} = 1 + 2\varepsilon_a + 3\varepsilon_a^2 + 4\varepsilon_a^3 + \dots, \quad (60)$$

$\hat{\varepsilon}_a$ would be modified by

$$\hat{\varepsilon}'_a \approx \hat{\varepsilon}_a - 1.5\hat{\varepsilon}_a^2 - 2\hat{\varepsilon}_a^3. \quad (61)$$

Equation (61) indicates that $|\hat{\varepsilon}_a|$ must satisfy

$$|\hat{\varepsilon}_a| \geq 1.5|\hat{\varepsilon}_a|^2 + 2|\hat{\varepsilon}_a|^3, \quad (62)$$

It means that $|\hat{\varepsilon}_a| \leq 0.43$, and the maximum detectable azimuth velocity will be

$$|V_{a,\max}| \approx 0.43V_p. \quad (63)$$

6. EXPERIMENTS AND RESULTS

6.1. Computer Simulation Results

We confirmed the proposed scheme by dozens of simulations. A typical experiment is presented herein. The radar system parameters in use are shown in Column 2 of Table 1.

In the simulation, the scene is a patch of terrain near Kunyu-Mountain, Shandong, China. Six moving targets, all sized by 5 m in range and 3 m in azimuth, are added to the scene. The random velocity vectors of six targets are listed in Table 2. After the simulated returns are collected and processed, a complex-valued SAR image is generated, and its amplitude image is presented in Figure 6. It can be seen that

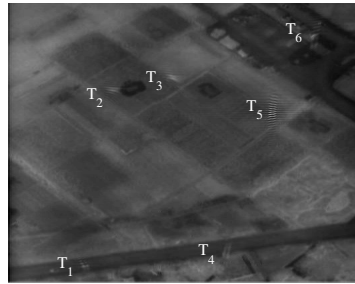


Figure 6. A simulated scene embedded with six moving targets.

Table 2. Simulation parameters and estimated results.

Target	Real Velocities [m/s]		Rough Estimates [m/s]			Final Estimates [m/s]			
	V_r	V_a	V_r	V_{a1}	V_{a2}	V_{r1}	V_{r2}	V_{a1}	V_{a2}
	T ₁	-8.0	10.0	-8.5170	10.6	10.7362	-7.6381	-7.7020	10.3
T ₂	20.0	-2.0	18.9961	-5.6	-1.6840	20.0748	19.3214	-5.6	-1.7050
T ₃	16.0	-6.0	15.0824	-6.3	-5.7242	16.0476	15.9948	-6.2	-5.9606
T ₄	4.0	15.0	5.0326	15.5	17.8935	4.2828	4.2964	15.4	15.2057
T ₅	2.0	20.0	2.7378	21.1	24.5542	2.1906	2.2351	21.1	19.2922
T ₆	5.0	25.0	7.6872	26.0	35.3839	5.8118	5.9679	25.7	23.7787

the moving targets are smeared and appear in displaced locations along azimuth direction.

We detect the moving targets by symmetric defocusing filters and isolate from the SAR image. Both range and azimuth velocity estimators are used to process each isolated patch. The velocity estimation results are listed in Table 2.

Let's discuss the elements in Table 2. The coarse range velocity estimates in Column 4 are estimated by Radon transform with the angle θ ranges from 0° to 179.9° with increment of 0.2° . Then we compensate the target patches by using these coarse range velocity estimates. As for the AVE based on symmetric defocusing technique (called AVE-I, for simplicity), the probing azimuth velocity ΔV_a ranges from 0 m/s to 30 m/s with increment of 0.1 m/s. The resulted coarse azimuth estimates are listed in Column 5. As for the AVE based on phase gradient technique (called AVE-II, for simplicity), it estimates each azimuth velocity component by both LS and ML methods, resulting in $\hat{V}_{a,LS}$ and $\hat{V}_{a,ML}$, respectively. The average of $\hat{V}_{a,LS}$ and

$\hat{V}_{a,ML}$, i.e., $(\hat{V}_{a,LS} + \hat{V}_{a,ML})/2$, is regarded as a coarse azimuth velocity estimate of a moving target. The six azimuth velocity estimates are listed in Column 6.

The modified range velocity components corresponding to the elements in Column 5 are listed in Column 7. The modified azimuth velocity estimates of the AVE-I are shown in Column 9, and that of the AVE-II are shown in Column 10. The modified range velocity components corresponding to the elements in Column 10 are listed in Column 8. We see that the AVE-II is more accurate than the AVE-I in the case of low azimuth speed because the sharpnesses of two defocused images differ slightly, and thus its feature curve is so smooth that the peak position is difficult to be determined. However, the AVE-I gives higher accuracy than the AVE-II does in the case of high azimuth velocity because the sharpnesses of two defocused images differ significantly, and thus the peak position of its feature curve is easily identified. As for the AVE-II, the skewer the phase gradient line, the larger the slope estimation deviation becomes.

6.2. Results of Field Data

A field complex-valued SAR image is collected near an airport in Shaanxi, China, as shown in Figure 7. The radar system parameters are shown in Column 3 of Table 1. The scene covers an area of about 765 meters in azimuth and 600 meters in range. Two vehicles, labeled by T_1 and T_2 , are arranged to moving along the runway in the same direction. Both vehicles move at the speed of 5 m/s approximately. The flight line of the platform parallels the runway. It can be seen that the background is focused fairly well while the image of the two vehicles are smeared due to their azimuth motion.

We detect the moving targets by using symmetric defocusing

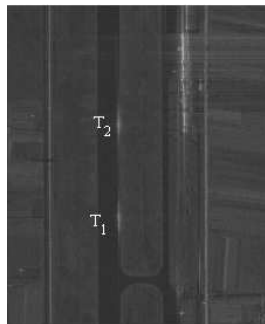


Figure 7. A SAR image containing two moving targets.

technique, and then isolate them from the SAR image. The target's velocity vector is computed on each isolated patch individually. The range Doppler plane of the patch containing T_1 is shown in Figure 8(a). By taking the Radon transform of Figure 8(a) with θ ranging from 0° to 179.8° increased by 0.2° , a Radon plane is achieved and shown in Figure 8(b). It can be seen that the angle corresponding to the Doppler locus is nearly concentrated in $\theta = 0^\circ$. By computing the standard deviation of the Radon plane along ρ axis at each θ point, a standard deviation curve varying with θ is obtained and shown as a dash line in Figure 9(a). As a result, $\hat{\theta} = 0^\circ$, and thus $\hat{V}_r = 0$ m/s.

The AVE-I uses an SDF bank with ΔV_a ranging from 0 to 30 m/s increased by 0.1 m/s. The resulted sharpness difference curve is normalized and shown as a dash line in Figure 9(b). The curve tells that the target is moving in an opposite direction of the radar platform, and the azimuth velocity estimate is about $\hat{V}_{a1} = -4.9$ m/s.

The same operations are applied to the patch containing T_2 .

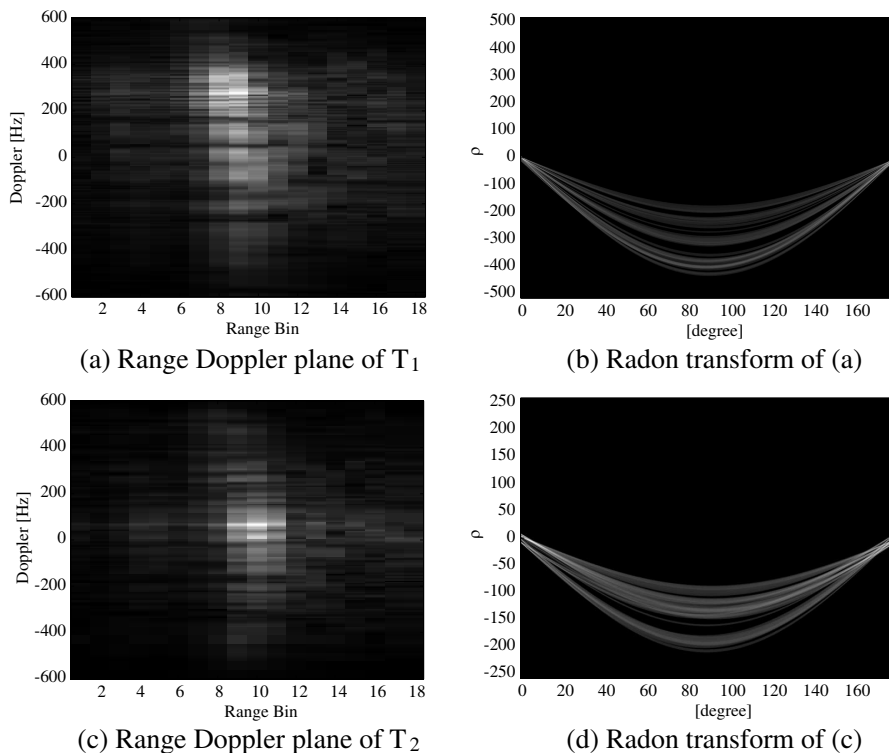


Figure 8. Range Doppler and Radon planes of T_1 and T_2 .

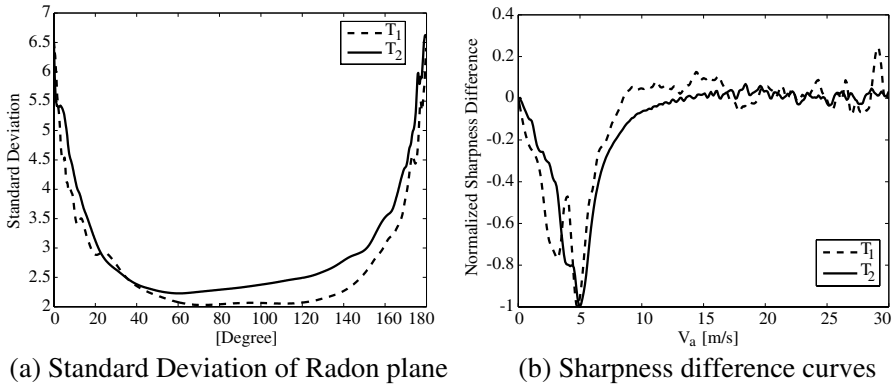


Figure 9. Feature curves of T_1 and T_2 .

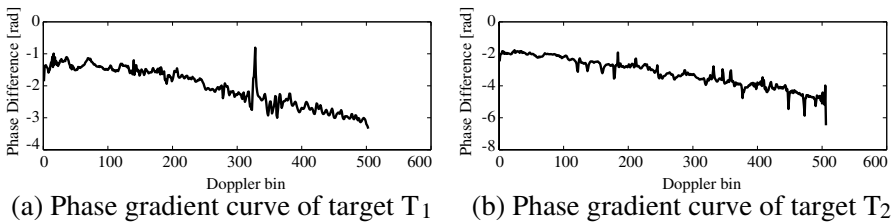


Figure 10. Phase gradient curves of targets T_1 and T_2 .

Figures 8(c) and (d) show its range Doppler plane and the Radon plane, respectively. The standard deviation curve used to compute the range velocity is shown in Figure 9(a), and the normalized sharpness difference curve used to compute the azimuth velocity is shown in Figure 9(b). As a result, its azimuth velocity estimate is about $\hat{V}_{a2} = -5.0$ m/s.

The AVE-II is also verified based on this image. For each isolated target patch, its range Doppler plane is compensated by its range velocity estimate first. Then the phase gradient in each range bin is computed. Figures 10(a) and (b) present two typical phase gradient curves for target T_1 and T_2 , respectively. For target T_1 , its final azimuth velocity estimates are $\hat{V}_{a1,LS} = -4.7443$ m/s and $\hat{V}_{a1,ML} = -4.8211$ m/s for LS and ML method, respectively. For target T_2 , its azimuth velocity estimates are $\hat{V}_{a2,LS} = -5.2948$ m/s and $\hat{V}_{a2,ML} = -5.1762$ m/s.

To present the effectiveness of the estimators further, we isolate two patches from a SAR imagery which generated by using the radar

parameters listed in Column 3 of Table 1, each of them contains an moving target with unknown velocity components. The patches are shown in Figures 11(a) and (b), denoted by T_{u1} and T_{u2} , respectively. The corresponding range Doppler loci are presented in Figures 11(c) and (d).

After taking Radon transform on Figures 11(c) and (d), the slopes of the range Doppler loci are calculated. As a result, the coarse range velocity components of target T_{u1} and T_{u2} are 21.65 m/s and 17.81 m/s, respectively. After aligned by the two coarse estimates, the range Doppler planes are refocused and used to estimate their azimuth velocities by the two AVEs. For target T_{u1} , its sharpness difference curve and phase gradient curve are shown in Figure 12(a). Its azimuth velocity estimate results are -1.5 m/s and -1.61 m/s for the AVE-I and the AVE-II, respectively, and the final range velocity is about 21.96 m/s. For target T_{u2} , its sharpness difference curve and phase gradient curve are shown in Figure 12(b). Its azimuth velocity

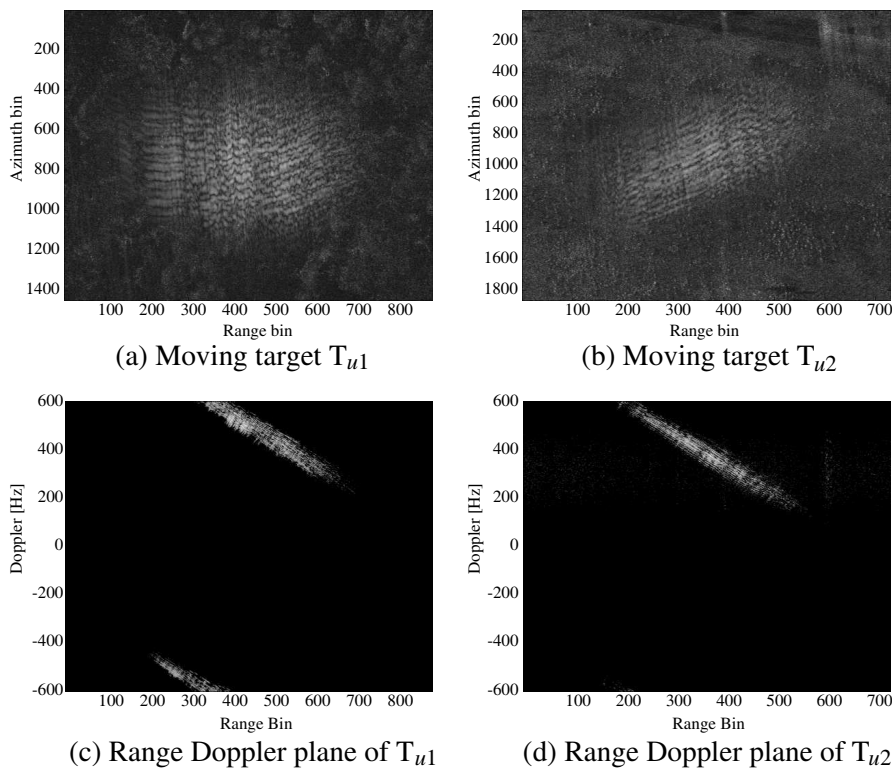


Figure 11. Two moving targets and their range Doppler planes.

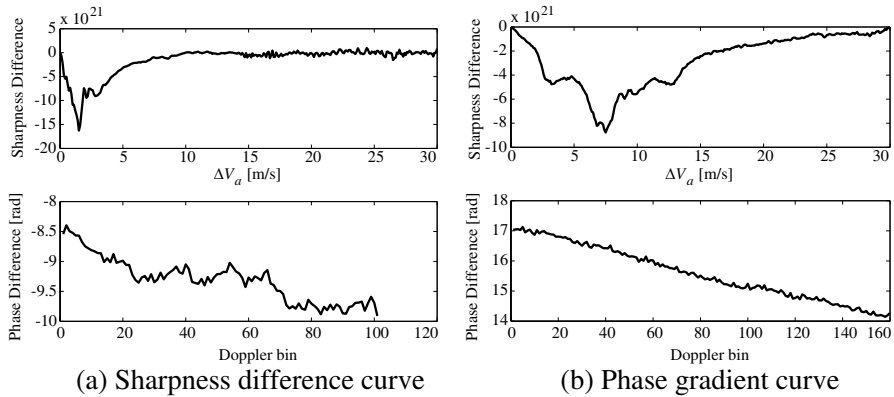


Figure 12. Feature curves of targets T_{u1} and T_{u2} .

estimate results are -7.5 m/s and -7.73 m/s for the AVE-I and the AVE-II, respectively, and the final range velocity is about 19.07 m/s. These estimates are reasonable in the reality.

7. CONCLUSION

New algorithms are proposed to estimate the velocity of a detected moving target in a complex-valued SAR imagery. The estimators are verified and confirmed by experiments with simulated and field data. They work effectively in the experiments.

The range velocity component is derived from the slope of the Doppler locus achieved through Radon transform directly, so this range velocity estimator need not resolve Doppler ambiguity. The estimated range velocity component should be modified to be more accurate by the azimuth velocity estimate.

Two azimuth velocity estimators are designed. One is based on symmetric defocusing, the other is based on phase gradient technique. The former is robust because it tries to alleviate the influence of clutters and interferences. The latter is sensitive to the clutters because it is based on estimation algorithms such as least square and maximum likelihood method. In practice, one can improve the latter's robustness by excluding the background from the detected target patch as much as possible. The former gives accurate estimate for an azimuth velocity larger than 2 m/s because the larger the azimuth velocity, the larger the sharpness difference becomes. The latter gives accurate estimate for an azimuth velocity lower than 20 m/s because the lower the azimuth velocity, the smaller estimation deviation of the phase gradient's slope is.

It should be pointed out that the proposed velocity estimators are not more accurate than that using multi-antenna systems or waveform diversity techniques. However, our estimators are more cost-effective for their simplicity and effectiveness.

ACKNOWLEDGMENT

We appreciate the support from the Shandong Young Scientists Award Foundation (Grant Number: BS2010DX021) and the National Natural Science Foundation of China (Grant Number: 61070175).

REFERENCES

1. Raney, R. K., "Synthetic aperture imaging radar and moving targets," *IEEE Transactions on Aerospace and Electronic Systems*, Vol. AES-7, No. 3, 499–505, 1971.
2. Barbarossa, S., "Detection and imaging of moving objects with synthetic aperture radar," *IEE Proceedings F Radar and Signal Processing*, Vol. 139, No. 1, 77–88, 1992.
3. Dias, J. and Marques, P., "Multiple moving targets detection and trajectory parameters estimation using a single SAR sensor," *IEEE Transactions on Aerospace and Electronic Systems*, Vol. 39, No. 2, 604–624, 2003.
4. Hinz, S., F. Meyer, A. Laika, and R. Bamler, "Spaceborne traffic monitoring with dual channel synthetic aperture radar-theory and experiments," *Proceedings of IEEE Computer Society Conference CVPR*, Vol. 13, 57–65, San Diego, USA, 2005.
5. Weihing, D., S. Hinz, F. Meyer, A. Laika, and R. Bamler, "Detection of along-track ground moving targets in high resolution spaceborne SAR images," *ISPRS Journal of Photogrammetry and Remote Sensing*, Vol. 61, Nos. 3–4, 135–140, 2006.
6. Hinz, S., F. Meyer, M. Eineder, and R. Bamler, "Traffic monitoring with spaceborne SAR-theory, simulations, and experiments," *Computer Vision and Image Understanding*, Vol. 106, Nos. 2–3, 231–244, 2007.
7. Chan, Y. K. and V. C. Koo, "An introduction to synthetic aperture radar (SAR)," *Progress In Electromagnetics Research B*, Vol. 2, 27–60, 2008.
8. Baumgartner, S. V. and G. Krieger, "Acceleration-independent along-track velocity estimation of moving targets," *IET — Radar, Sonar and Navigation*, Vol. 4, No. 3, 474–487, 2009.

9. Wong, S. K., "High range resolution profiles as motion-invariant features for moving ground targets identification in SAR-based automatic target recognition," *IEEE Transactions on Aerospace and Electronic Systems*, Vol. 45, No. 3, 1017–1039, 2009.
10. Chiu, S. and M. V. Dragošević, "Moving target indication via Radarsat-II multichannel synthetic aperture radar processing," *EURASIP Journal on Advances in Signal Processing*, Vol. 2010, 1–19, Article ID 740130, 2010.
11. Baumgartner, S. V. and G. Krieger, "Real-time road traffic monitoring using a fast a priori knowledge based SAR-GMTI algorithm," *Proceedings of IEEE IGARSS*, Honolulu, USA, 2010.
12. Chang, C. Y., Y. L. Chiang, and K. S. Chen, "SAR image simulation with application to target recognition," *Progress In Electromagnetics Research*, Vol. 119, 35–57, 2011.
13. Koo, V. C., Y. K. Chan, G. Vetharatnam, M. Y. Hua, C. H. Lim, C.-S. Lim, C. C. Thum, T. S. Lim, Z. bin Ahmad, K. A. Mahmood, M. H. Bin Shahid, C. Y. Ang, W. Q. Tan, P. N. Tan, K. S. Yee, W. G. Cheaw, H. S. Boey, A. L. Choo, and B. C. Sew, "A new unmanned aerial vehicle synthetic aperture radar for environmental monitoring," *Progress In Electromagnetics Research*, Vol. 122, 245–268, 2012.
14. Friedlander, B. and B. Porat, "VSAR: A high resolution radar system for ocean imaging," *IEEE Transactions on Aerospace and Electronic Systems*, Vol. 34, No. 3, 755–776, 1998.
15. Budillon, A., V. Pascazio, and G. Schirinzi, "Estimation of radial velocity of moving targets by along-track interferometric SAR systems," *IEEE Geoscience and Remote Sensing Letters*, Vol. 5, No. 3, 349–353, 2008.
16. Tian, B., D. Y. Zhu, and Z. D. Zhu, "A novel moving target detection approach for dual-channel sar system," *Progress In Electromagnetics Research*, Vol. 115, 191–206, 2011.
17. Fan, C. Y., X. T. Huang, T. Jin, J.-G. Yang, and D. X. An, "Novel pre-processing techniques for cohenrence improving in along-track dual-channel low frequency sar," *Progress In Electromagnetics Research*, Vol. 128, 171–193, 2012.
18. Gierull, C. H., "Ground moving target parameter estimation for two-channel SAR," *IET — Radar, Sonar and Navigation*, Vol. 153, No. 3, 224–233, 2006.
19. Moreira, J. R. and W. Keydel, "A new MTI-SAR approach using the reflectivity displacement method," *IEEE Transactions on Geoscience and Remote Sensing*, Vol. 33, No. 5, 1238–1244, 1995.

20. Ender, J., "Detection and estimation of moving target signals by multichannel SAR," *Proceedings of EUSAR*, 411–417, Königswinter, Germany, 1996.
21. Kirsht, M., "Detection, velocity estimation and imaging of moving targets with single-channel SAR," *Proceedings of EUSAR*, 587–590, Friedrichshafen, Germany, 1998.
22. Kersten, P. R., R. W. Jansen, K. Luc, and T. L. Ainsorth, "Motion analysis in SAR images of unfocused objects using time-frequency methods," *IEEE Geoscience and Remote Sensing Letters*, Vol. 4, No. 4, 527–531, 2007.
23. Wang, J. F. and X. Z. Liu, "Velocity estimation of moving targets using SAR," *Proceedings of IEEE IGARSS*, Vancouver, Canada, 2011.
24. Marques, P. and J. Dias, "Velocity estimation of fast moving targets using a single SAR sensor," *IEEE Transactions on Aerospace and Electronic Systems*, Vol. 41, No. 1, 75–89, 2005.
25. Marques, P. and J. Dias, "Moving targets processing in SAR spatial domain," *IEEE Transactions on Aerospace and Electronic Systems*, Vol. 43, No. 3, 864–874, 2007.
26. Legg, J., A. Bolton, and D. Gray, "SAR moving target detection using non-uniform PRI," *Proceedings of EUSAR*, 423–426, Königswinter, Germany, 1996.
27. Rüegg, M., E. Meier, and D. Nüesch, "Capabilities of dual-frequency millimeter wave SAR with monopulse processing for ground moving target indication," *IEEE Transactions on Geoscience and Remote Sensing*, Vol. 45, No. 3, 539–553, 2007.
28. Brush, S., S. Lehner, T. Fritz, M. Soccorsi, A. Soloviev, and B. Schie, "Ship surveillance with TerraSAR-X," *IEEE Transactions on Geoscience and Remote Sensing*, Vol. 49, No. 3, 1092–1103, 2011.
29. Fienup, J. R., "Detecting moving targets in SAR imagery by focusing," *IEEE Transactions on Aerospace and Electronic Systems*, Vol. 37, No. 3, 794–809, 2001.
30. Cumming, I. G. and S. Li, "Improved slope estimation for SAR Doppler ambiguity resolution," *IEEE Transactions on Geoscience and Remote Sensing*, Vol. 44, No. 3, 707–718, 2006.